Mass loss simulation in cavitation erosion: fatigue criterion approach

Regiane Fortes-Patella, Thierry Choffat, Jean-Luc Reboud, Antoine Archer

Mass loss simulation in cavitation erosion: Fatigue criterion approach

Regiane Fortes Patella [a,*], Thierry Choffat [a], Jean-Luc Reboud [b], Antoine Archer [c]

[a] LEGI—Grenoble INP, BP 53, 38041 Grenoble Cedex 9, France
[b] G2ELAB, University of Grenoble, BP 166, 38042 Grenoble Cedex 9, France
[c] EDF R&D, 78401 Chatou, France

As a complement to previous works developed in laboratory LEGI[1] to model and simulate cavitation erosion phenomenon [1–6] (Fortes-Patella and Reboud, 1998; Fortes Patella et al., 2000; Fortes Patella et al., 2001; Fortes Patella et al., 2012; Choffat et al., 2003), a 2D axi-symmetric dynamic approach based on fatigue criterion was proposed and applied to predict cavitation erosion of aluminium 1050A, copper 99.99% and 316L stainless steel samples.

The proposed physical model is based on an oligocyclic fatigue approach, with the Palmgreen–Miner rule for damage accumulation. The stress loading applied by the cavitating flow is deduced from results of pitting measurement made in previous works [3,6] (Fortes Patella et al., 2000; Choffat et al., 2003). The behaviour of the material exposed to cavitation loading was implemented in a simulation tool in the scope of collaborations with EdF-R&D.[2] This tool predicts material damage by calculating the material removal rate.

Making use of the experimental data supplied by EdF-R&D, analyses were done in order to study the influence of physical and simulation parameters on quantitative results. For the few known experimental data, simulated damage rates are found in satisfactory agreement with measured ones. The relationship between erosion rates and pitting rates was also studied.

1. Introduction

The study and the prediction of cavitation erosion phenomenon are very complex because of hydrodynamic, mechanical, metallurgical and chemical behaviours interactions. Consequently, scenarios taking into account these phenomena and their interactions have to be developed to accurately predict the erosion of a material exposed to a cavitating flow through time.

Some works made in order to predict cavitation erosion established, for specific conditions, experimental correlations between one or more mechanical properties of the materials (such as their yield strength or hardness) and their erosion through time [7–16].

Other approaches intended to predict the erosion of a material exposed to a cavitating flow using data that can be obtained from pitting tests, as for example proposed by [17–18]. These tests are made during the incubation period (the material sustains elasto-plastic deformation, without mass loss). Their aim is to provide the geometrical characteristics of the pits generated by the cavitation impacts to deduce the characteristics of the pressure loadings endured by the solid, and thus, to evaluate the cavitating flow aggressiveness. The idea to use the material as a sensor was proposed by [19] because of the difficulty to get precise information using other measurement systems: the time scale, of the order of 10 ns, is too short to enable proper answer of gauges; the spatial resolution is also problematic, because the active surface of the sensor must be smaller than the dimension of the impact in order not to underestimate it by averaging the pressure pulse on the whole surface of the sensor. Pitting tests are today widely used to process erosion prediction [20–22].

By using pitting tests data, Karimi and Leo [17] proposed a static one-dimensional model based on work-hardening of the materials. It considers the assumption that pressure loadings progressively lead to the work-hardening of the material, until it cannot sustain any energy supply and thus breaks, leading to the erosion of the material. That model was applied by [18,20,21].

Our research team has been working for many years to propose, implement and validate physical models in order to improve knowledge and prediction of material damage due to cavitation. In previous works [1–5] a physical scenario and a numerical approach have been proposed to model and to analyse the cavitation erosion phenomena at the bubble scale. Numerical simulations taking into account the coupling between flow aggressiveness and material characteristics were proposed and

* Corresponding author. Tel.: +33 476825081; fax: +33 4 76825271.
E-mail addresses: regiane.fortes@legi.grenoble-inp.fr (R. Fortes Patella), jean-luc.reboud@ujf-grenoble.fr (J.-L. Reboud), antoine.archer@edf.fr (A. Archer).

[1] Laboratoire des Ecoulements Géophysiques et Industriels, France.
[2] Electricité de France.

Nomenclature

C coefficient of the fatigue energy criterion (J/m^3)
C_{liq} wave celerity (m/s)
D damage function (-)
dt wave passage time (s)
e_{int} energy density of residual internal stresses (J/m^3)
E_{pl} residual plastic energy (J)
E_{pot} potential energy of the vapour cavity (J)
E_{wave} impacting pressure wave energy (J)
$pE^p = \rho\, V_{\mathrm{er}}$ steady-state erosion rate (μg/mm^2/s)
$g(r)$; $g(z)$ Gauss function (-)
H maximum depth of a pit (m)
L distance of wave emission centre from solid boundary (m)
N_r number of cycles to rupture under cyclic loading (-)
P wave peak pressure applied to solid surface (Pa)
r radial position in the mesh (m)
$R_{10\%}$ radius of a pit at 10% of its maximum depth (m)
T_i incubation time (s) or (h)
v flow velocity (m/s)
V_{pit} volume of a pit (m^3)
V_d pitting rate (μm^3/mm^2/s)
$V_{\mathrm{er}} = \dot{E}/\rho$ volumic erosion rate (μm^3/mm^2/s)
z mesh depth (m)
$\alpha = \frac{E_{pl}}{V_{pit}} = \eta_{solid/wave}\beta$ parameter based on material elastoplastic property (J/mm^3)
$\beta = \frac{E_{wave}}{V_{pit}}$ parameter based on material elastoplastic response (J/mm^3)
$\chi = \frac{\eta_{solid/wave}\gamma_{n/1}\beta}{C}$ model dimensionless parameter (-)
δ exponent of the fatigue energy criterion (-)
ΔD damage increment (-)
Δe_{int} increment of energy density of residual internal stresses (J/m^3)
$\dot{\varepsilon}$ strain rate tensor (s^{-1})
$\gamma_{n/1}$ ratio between the energy increment after n impacts and after the first impact (hardening phenomenon parameter) (-)
$\lambda = \frac{C_{liq}dt}{L}$ dimensionless wave passage time (-)
$\eta_{solid/wave} = \frac{E_{pl}}{E_{wave}}$ erosive efficiency (-)
$\eta_{\mathrm{wave/buble}} = \frac{E_{wave}}{E_{pot}}$ bubble collapse efficiency (-)
ρ specific mass of the material (kg/m^3)
ρ_{liq} specific mass of the liquid (kg/m^3)
σ stress tensor (Pa)
σ_{cav} cavitation number $\sigma_{\mathrm{cav}} = (P_{\mathrm{downstream}} - P_{\mathrm{vapor}})/(0.5\rho_{\mathrm{liq}}\, v^2)$ (-)

applied mainly to study incubation period of cavitation damage, that is to say only the elasto-plastic behaviour of the material, without any mass loss [23].

To meet the industrial needs for damage prediction, the step between pitting to mass loss must then be examined.

Based on those previous studies and developed tools, and as a complement of them, the present paper proposes a new approach to evaluate mass loss of different materials exposed to cavitating flows. In Section 2 of the paper, the proposed physical scenario and tools previously developed are summarized.

The physical model applied to predict mass loss period of cavitation erosion phenomenon is detailed in Section 3. Initial applications and qualitative analyses of obtained results are illustrated in Section 4. Section 5 presents influence tests of model parameters. Comments about relationship between erosion rates (obtained during mass loss period) and pitting rates (evaluated from pitting tests made during incubation period) are exposed in details in Section 6. Section 7 presents comparison of simulation results with experimental values of incubation time and steady-state erosion rate.

2. Scope and tools

2.1. Physical model of cavitation erosion

Numerical studies from [1] allowed analysing the shape of the pits resulting from microjet and pressure wave loadings. The pressure wave emission from bubble collapse at very close proximity of the solid surface has been assessed to be the mechanism responsible for the erosion of materials exposed to cavitating flows. Thus the proposed physical scenario considers that the cavitation erosion is caused by the impacts of high pressure waves emitted during the collapse of vapour structures. Transient interaction of pressure wave and elasto-plastic behaviour of the solid results in residual pit on the solid surface. Pit size and depth depend on the pressure wave and material characteristics. Using these previous numerical simulations it was found possible to associate a spherical pressure wave with each observed pit shape. That pressure wave is characterized by an emission distance L from the material surface, a maximum amplitude P and a passage time dt.

2.2. Energy approach from fluid flow to material pitting

With the help of numerical simulations, an energy balance between vapour structures, pressure waves and the solid material can be proposed to analyse the incubation period of cavitation damage. The applied physical scenario is summarized in Fig. 1

- the vapour cavity has a potential energy E_{pot}
- during the vapour structure collapse, a pressure wave is emitted and hits the material surface. The energy of the pressure wave is referred to as E_{wave}
- the pressure wave impacting the solid boundary deforms it plastically. The residual plastic energy E_{pl} is a fraction $\eta_{solid/wave}$ of E_{wave}
- if the material is free from previous impacts in the pressure wave area (that means there is no pits overlapping), the volume V_{pit} of the residual pit is related to E_{pl} as

$$E_{pl} = \alpha V_{pit} \tag{1}$$

where α depends on the material mechanical characteristics. We can also write

$$E_{wave} = \frac{\alpha}{\eta_{solid/wave}} V_{pit} = \beta V_{pit} \tag{2}$$

According to [5], $\beta_{\mathrm{aluminium}} = 4$ J/mm^3, $\beta_{\mathrm{copper}} = 20$ J/mm^3, and $\beta_{316L\ SS} = 24$ J/mm^3.

2.3. Pitting simulation tools

To simulate interaction between pressure wave and material surface a numerical model of the dynamic impact response of an elasto-plastic medium subjected to a spherical pressure wave impact was developed [25], and improved [1], using the finite element methods in 2D axi-symmetric configurations. The

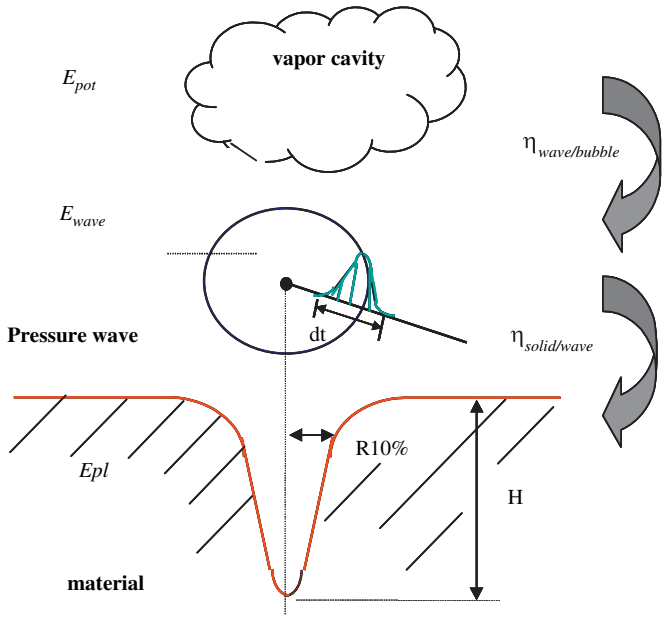

Fig. 1. Scheme of the proposed physical model: pressure wave emitted during the collapse of vapor structures seems to be the phenomenon responsible for material damage. The collapse of vapor cavities is characterized by potential energy E_{pot} (related to the pressure gradient and to the cavity volume) and by collapse efficiency $\eta_{wave/bubble}$; the emitted pressure wave is characterized by the acoustic energy E_{wave}; the material damage is described by the indentation volume $V_{pit}=f(R_{10}\%,H)$ [5,24].

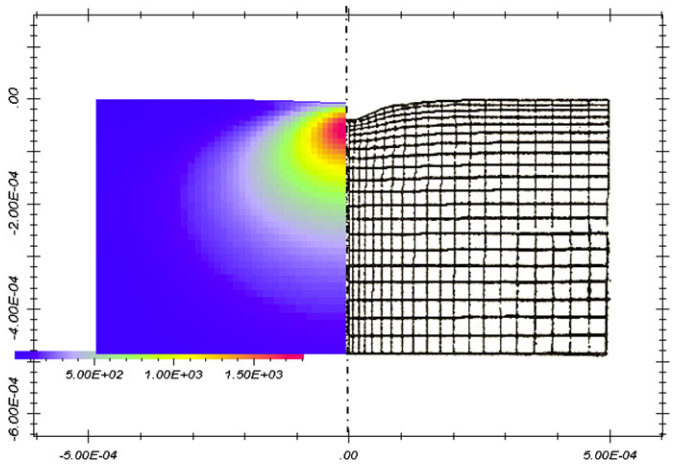

Fig. 2. Final state of stainless steel material after the impact of a pressure wave on its surface. Left side: Residual energy density of internal stresses e_{int} (J/m^3). Right side: Mesh deformation, amplified by a factor 20 in r and z direction. Pressure wave characteristics: maximum amplitude $P=1.5$ GPa, emission distance from the boundary $L=0.1$ mm, passage time $dt=1.8$ μs. The co-ordinates are cylindrical axi-symmetric. For more information about numerical code, see [1].

software provides the complete transient evolution of the material (strain, stress and energy fields) and the final surface deformations (the pit profiles). Moreover, it enables to calculate the energy density of internal stresses per volume unit remaining in a solid after a transient pressure impingement (Fig. 2).

According to numerical calculations, the maximum of the residual internal stresses is located on the axis of symmetry, but not at the surface of the material. As in the case of Hertz theory, the maximum residual stress is located below the material surface ($z<0$), at a depth depending on the loading shape.

Using numerical calculations, by considering several materials and different pressure wave characteristics, ratio β between the pressure wave energy E_{wave}, and the volume of the residual pit V_{pit} was found approximately constant for a given material [4,26].

Therefore, thanks to previous simulations [1], the characteristics (in particular E_{wave}) of the pressure waves responsible for the generation of an isolated pit can be determined from the geometric characteristics of the pit (radius, depth and volume). After measuring the depths on a target previously mirror-polished and then exposed to a cavitating flow during incubation period, a software developed in our team locates the pits, evaluates their geometric characteristics, and calculates the properties of the pressure waves [3].

2.4. Determination of a representative hydrodynamic loading

An accurate estimation of the pressure wave characteristics and correct counting of impacts on a solid surface submitted to cavitating flow requires the pits to be isolated (or at least not too many of them being superposed). Thus, pitting tests must be short enough to avoid too many overlapping, but long enough to get a good statistic population of the impacts endured by the material. To partially take into account the practical experimental constraints, correction methods to account for overlapping are proposed and discussed in [6].

After getting a statistic population of pressure waves emitted by the cavitating flow and damaging the target, simulations can be done to evaluate the mass loss through time. This requires calculating how the material evolves when it is impacted, and how the mass loss occurs. In this way, a software was developed to simulate the generation of cavitation impacts on a solid surface. From a pitting test concerning a material exposed to a given cavitation condition during the test duration, the software predicts the damage of this material exposed to the same cavitating flow as time goes. Results can be transposed to other materials. The fracture model implemented in the simulation tool to evaluate mass loss is detailed in Section 3.

3. Fatigue erosion model

The proposed damage model takes into account fatigue phenomena. We consider that cavitation erosion occurs after repeated pressure loadings on the metal, in the range of its plastic deformation, as attested by observations of permanent indentations on the solid surfaces. Thus the model assumes that the mechanism responsible for metal rupture is oligocyclic fatigue. This assumption agrees with experimental observations presented by [27–33]. Those authors observed that the morphology of cavitation wear was comparable to one characterized by fatigue damage. Moreover, from tests and analyses performed by [34], it appeared that there was correlation between fatigue strength of the material under random loading and its cavitation erosion resistance.

Please note that the model includes also the work-hardening phenomenon under oligocyclic loads (see Section 3.2.2).

3.1. Assessed material behaviour

Rupture happens when a material is loaded beyond its rupture limit. However, metals can break if they endure cyclic loadings, even though these loadings remain under the rupture limit of the material or even its elastic limit. This is due to the progressive propagation of microcracks on the metal at each loading cycle. This phenomenon is referred to as fatigue [35,38].

When the material is loaded between its elastic limit and its rupture limit, the process is called oligocyclic fatigue, because the material sustains global plastification at each cycle, which leads to its rupture after few cycles. The rupture of a metal loaded in fatigue

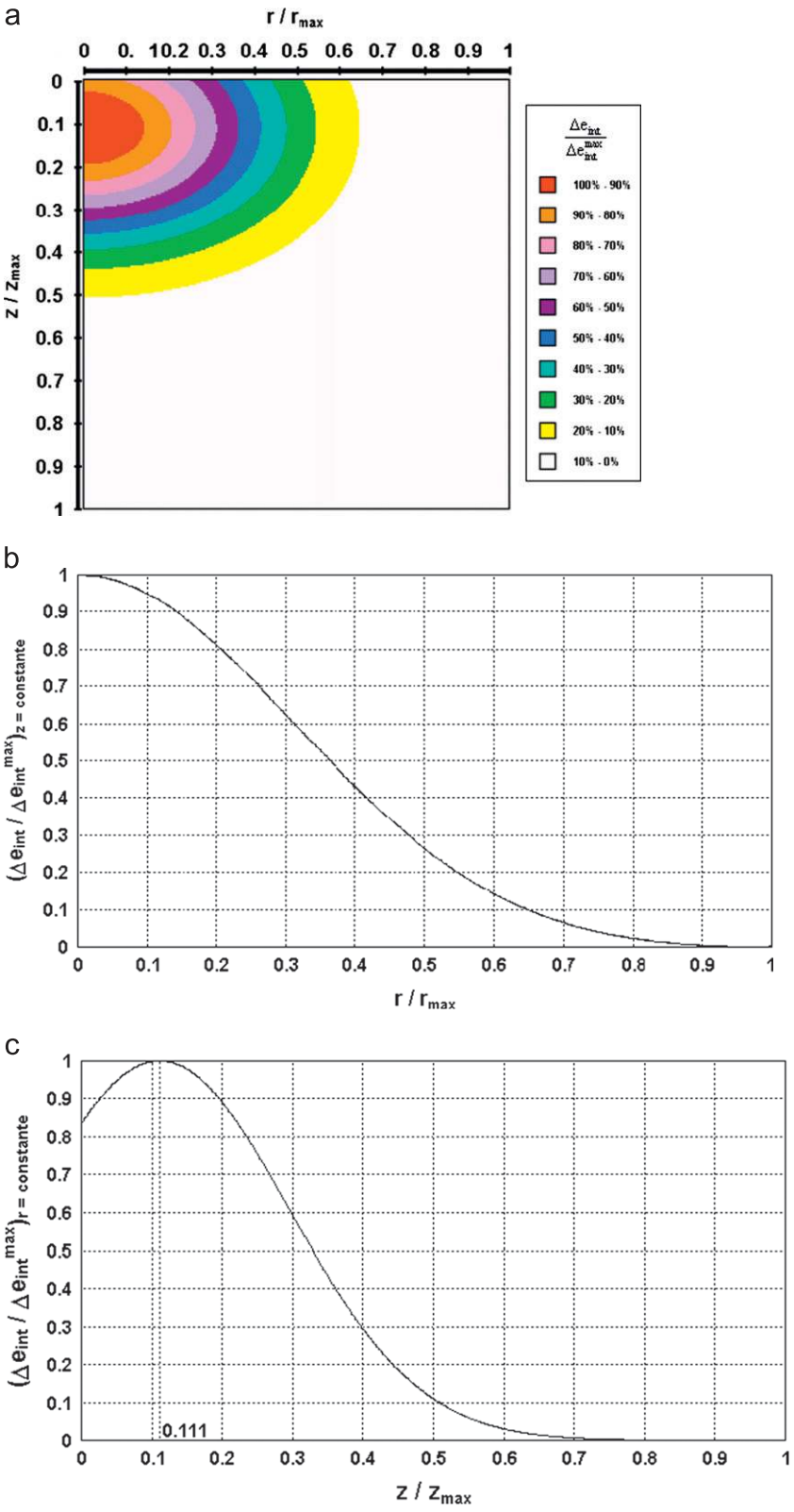

Fig. 3. Dimensionless repartition of the residual energy density of internal stresses. From several numerical results as one illustrated in Fig. 2, an averaged axi-symmetric dimensionless distribution of energy density has been obtained. (a) Two-dimensional axi-symmetric distribution observed in the material after a pressure wave impact. (b) Distribution of dimensionless energy density in the radial direction for a constant depth. (c) Distribution of dimensionless energy density in the depth direction along the axis of symmetry. As indicated in Section 2.3, according to our numerical simulations, the maximum value of residual stresses energy density is obtained at the depth $z=(1/9)z_{max}$, where z_{max} is the maximum depth affected by plastic deformation due to pressure wave impact.

happens after a given number N_r of loading cycles which depends on the stress intensity $\Delta\sigma$ of the loading. This relationship is given by the Wöhler curve [36].

Taking into account microcracks propagation requires microstructural information and demanding calculations. This would be too complex and long, so the proposed model relies on a

simplified approach within the hypotheses of continuum mechanics. At each loading cycle, the material is supposed to be loaded over a given volume with different amplitude depending on the point considered, which sustains a particular damage increment. This damage notion renders the fact that the material evolves as it is loaded. Let us call $D(x,y,z)$ the function representing the local damage of the material. When the material is intact, $D=0$. At each loading cycle, the material endures a damage increment ΔD. The resulting increase of the damage of the material renders the decrease of its capacity not to break as it endures more loadings, until it can not resist anymore and eventually breaks when it is too much damaged: the damage value at rupture is $D=1$.

Different relationships can be proposed depending on the situation considered. The criterion adopted in the model is the energy criterion proposed by [37]. When a material endures cyclic loading, its stress–strain curve follows a cyclic behaviour; in the case of oligocyclic fatigue where global plastification occurs, the material becomes smoother or harder until it reaches a steady behaviour. Integral calculation enables to deduce the increment of the energy density of internal stresses,

$$\Delta e_{\text{int}} = \int_0^{\Delta t} \int_{Vs} (\sigma_{ij}\dot{\varepsilon}_{ij} dV) dt, \tag{3}$$

absorbed by the material at each cycle.

After a given number N_r of cycles, the material breaks. N_r is the number of cycles the material can endure before breaking when it absorbs an energy increment Δe_{int} at each cycle. In oligocyclic fatigue, which is supposed to be the case in cavitation erosion where pressure impulses can reach several GPa, N_r and Δe_{int} would be linked by the correlation proposed by [37]

$$\Delta e_{\text{int}} = \frac{C}{N_r^{\delta}} \tag{4}$$

Parameters C and δ are characteristic of the material. For example, from results presented in [38], we deduced for 316L stainless steel

$$C = 1.85 \times 10^9 \text{ J/m}^3 \quad \text{and} \quad \delta = 0.67$$

This criterion allows expressing the loading increment in terms of energy density, and is linked to the number of cycles before rupture.

The damage increment ΔD and its accumulation still remain to be defined. For this, we consider a simple situation: a material enduring constant cyclic loading, leading to its rupture after N_r cycles. If we suppose that each cycle evenly damages the material and that these damage increments can be linearly added, we get the following correlation at rupture: $N_r \times \Delta D = 1$. Consequently, the damage increment could be defined by

$$\Delta D = \frac{1}{N_r} \tag{5}$$

This definition is generalised to the case of loadings of different amplitude: If the material endures a loading that would lead to its rupture after N_i cycles, the damage increment is

$$\Delta D = \frac{1}{N_i}. \tag{6}$$

The cumulative damage is

$$D = \sum_i \frac{1}{N_i}. \tag{7}$$

When this value exceeds 1, the material breaks. This law is known as the Palmgreen–Miner rule [38,39]. It is important to note that this simple rule is characterized by a significant dispersion around the rupture value $D=1$, because of extreme complexity of fatigue phenomenon, characterized by its huge randomness and is influenced by microstructural aspects (defaults, phase changes, joint boundaries and others).

3.2. Calculation code

A calculation code has been developed to implement this model. The simulated sample is represented by a 3D mesh that is the discretized fluid–material surface and its depth. In each cell, the code will calculate the cumulative damage, generated by the fluid impact at this surface location.

3.2.1. The fluid loading as input data

To simulate mass loss, the model requires geometric data from pitting test analysis, which provides statistic population of the impacts endured by the material. A listing of volumes V_{pit} and radius $R_{10\%}$ of indentations measured by pitting tests are used as entries of the code. The calculation code takes indentations one by one in the pit listing, and randomly places them on the sample.

3.2.2. Cumulative energy inside the material

The repartition of the damage engendered by these impacts then has to be calculated.

First, the averaging of numerical results, as the one illustrated by Fig. 2, obtained with a large range of varying impact and material characteristics, provides axi-symmetric dimensionless energy density distribution illustrated by Fig. 3. Using this distribution, impact damage can be represented in two-dimensional axi-symmetric coordinates by

$$\Delta e_{\text{int}}(r,z) = \Delta e_{\text{int}}^{\max} f_r(r/r_{\max}) f_z(z/z_{\max}) \tag{8}$$

where $\Delta e_{\text{int}}^{\max}$ is the maximum increment of energy density, $r_{\max}$ is the maximum affected radius and $z_{\max}$ is the maximum affected depth.

As a matter of fact, making use of simulation code presented in Section 2, numerical tests have been carried out to calculate the evolution of energy density of internal stresses repartition in the case of repeated impacts of same characteristics and axis. It has been found that the shape of this repartition is close to the shape of the energy repartition after one impact. Repeated impacts of same axis but different characteristics have also been simulated: It has been found only a small influence in the shape of the energy density repartition.

It is important to note that impacts of different axis have not been simulated, because of the lack of 3D code. Consequently, we consider in the present work that the dimensionless energy repartition is the same whatever the situation is, and corresponds to that of identical repeated impacts of same axis.

For each simulated pit, maximum affected radius $r_{\max}$ and depth $z_{\max}$ can be related to pits measured radius $R_{10\%}$ and estimated distance L of pressure wave emission. The simplified expression of the repartition of the energy density increase becomes:

$$\Delta e_{\text{int}}(r,z) = \Delta e_{\text{int}}^{\max} g_r(r,R_{10\%},L') g_z(z,R_{10\%},L') \tag{9}$$

where r is the radial position, z the depth, and g a function close to a Gauss function (Fig. 3b and c).

The distance L' defined by

$$L' = L(\lambda/3.6)^{\frac{1}{3}} \tag{10}$$

is related to the distance L between the solid boundary and the emission location of the pressure wave and takes into account also the influence of pressure wave passage time ($\lambda = C_{liq}dt/L$).

In the present study, based on previous works [1], we consider

$$\frac{R_{10\%}}{L} = f(\lambda). \tag{11}$$

For the initial applications, we adopted the value $\lambda=12$. The influence of this parameter on damage prediction has been analysed and is presented on Section 5.

The damaged zone concerns a $r_{max}=4L'$ distance around the impact axis, and a $z_{max}=3L'$ distance from the surface. The maximum damage Δe_{int}^{max} is reached at a $L'/3$ distance from the surface on the axis of the impact. According to simulations performed, Δe_{int}^{max} is given by the correlation

$$\Delta e_{int}^{max} = \frac{\eta_{solid/wave}\gamma_{n/1}E_{wave}}{10L'^3} \tag{12}$$

E_{wave} is linked to the indentation volume by the relationship $E_{wave}=\beta V_{pit}$, where β could be calculated by previous numerical simulations and is constant for a given material [4,26].

As indicated in Section 2, parameter $\eta_{solid/wave}$ corresponds to the ratio between the energy deforming plastically the material and the energy of the pressure wave seen by the boundary. This parameter depends on the amplitude of the pressure wave [2,26]. However, for simplification purposes, an average value is used in the model for each considered material (Table 1). Results concerning influence tests are presented in Section 5.

Because of hardening phenomena under oligocyclic loads, parameter $\gamma_{n/1}$ is introduced

$$\gamma_{n/1} = \frac{\Delta e_{int}^{max}(n)}{\Delta e_{int}^{max}(1)} \tag{13}$$

where $\Delta e_{int}^{max}(1)$ is the increment of the energy density of internal stresses after the first impact, and $\Delta e_{int}^{max}(n)$ the corresponding increment of the energy density of internal stresses, after the nth impact. As illustrated in Fig. 4 in the case of stainless steel under repeated loads, the energy density increment decreases between the first impact and the others, to reach a constant value after few impacts. It gives in this case a $\gamma_{n/1}$ value close to 50%.

To summarize, in the proposed material fatigue damage simulation, the increment of energy density of internal stresses can be evaluated using pitting test results (volume and radius $R_{10\%}$ of the indentations) and corrected by the $\gamma_{n/1}$ parameter to account for repeated loads Table 2.

When this increment has been calculated, the damage increment can be deduced from the energy density increase as proposed in [37]

$$\delta D = \frac{1}{N_i} = \left(\frac{\Delta e_{int}}{C}\right)^{\frac{1}{\delta}} \tag{14}$$

The cumulative damage is then incremented

$$D(i+1) = D(i) + \delta D \tag{15}$$

If it exceeds 1, rupture is supposed to happen. Following this assumption, the material layer situated between the surface and the point where rupture happened is removed. It is worth noting that energy distribution is simulated by a 2D axi-symmetrical approach, but rupture criterion is based on one-dimensional assumption.

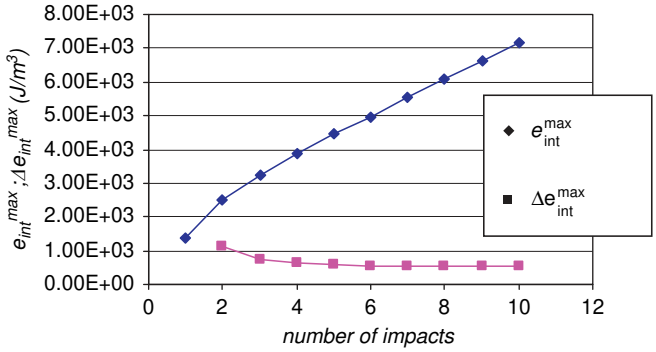

Fig. 4. Evolution of the maximum internal stresses energy density e_{int}^{max} after successive impacts (diamonds) on a stainless steel. The squares show the increment e_{int}^{max} between two successive impacts.

Table 2
Experimental conditions of aluminium pitting tests carried out in Modulab test rig at 30 °C [3].

Reference of pitting test	Exposure time (s)	Flow velocity (m/s)
Al234	10	32
Al233	20	32
Al232	30	32

Table 1
.V_{er} is obtained from Fig. 6b and Eq. (19).

Material	Reference of pitting test[a]	Flow velocity[a] (m/s)	Exposure time[a] (s)	Measured V_d[b] ($\mu m^3/mm^2/s$)	Calculated V_{er}[c] ($\mu m^3/mm^2/s$)	V_{er}/V_d (-)
Copper $\eta_{solid/wave}=5.2\pm1.6\%$	cu40	16	900	38.4	11.7	0.30
$\beta=20\pm2$ J/mm^3	cu27d	20	300	131	49.4	0.38
	cu29d	25	120	573	215	0.38
	cu30	25	120	456	217	0.48
	cu31d	32	60	1331	617	0.46
	cu32	32	60	1390	642	0.46
	cu39d	38.5	30	5280	2716	0.51
Stainless steel $\eta_{solid/wave}=5\pm0.6\%$	in17c	20	7200	1.73	0.7	0.40
$\beta=24\pm2$ J/mm^3	in25	25	3600	6	3.6	0.60
	in19	25	3600	7.2	4.4	0.61
	in21c	32.1	1800	26.5	18.2	0.69
	in16c	38.5	900	54.3	39.9	0.73
Aluminium $\eta_{solid/wave}=10\pm3\%$	al96	20	120	990	85.7	0.09
$\beta=4\pm0.5$ J/mm^3	al100	20	120	985	86	0.09
	al102	25	60	3120	285	0.09
	al104	32	30	10500	1210	0.12
	al106	38.5	21	22000	2960	0.13

[a] Experimental conditions of pitting tests [3].
[b] Corresponding measured values of V_d.
[c] Simulated V_{er} values.

4. Examples of application

4.1. Calculation conditions

To illustrate the results obtained by the developed code, we have used a pit listing corresponding to an aluminium 1050A pitting test carried out at EDF-R&D in the MODULAB test rig during 10 s (cavitation number $\sigma_{cav}=0.7$, flow velocity=32 m/s, temperature 30 °C). Samples were damaged by water cavitating flow downstream a diaphragm generating wake-cavitation (Fig. 5). A 3D laser profilometry technique was proposed to measure material damage due to cavitating flows. A software for automatic analysis of the sample surfaces pitted by cavitation was developed and used to treat experimental results. The in-house developed software provides the radius, depth and volume for every single indentation (pit) (for more details, see [3]). These pitting tests data are used as entries of the erosion calculation code.

The volume of the simulated surface is about 10 $mm^2 \times 330$ μm in depth; the step at the surface is 25 μm in both directions, and the step in depth is 4,2 μm. A detailed study to obtain satisfactory mesh convergence has been performed by [40].

The following material properties (316L SS) have been used for mass loss simulation

$\beta = 24\ J/mm^3 \quad \eta_{solid/wave} = 10\% \quad \gamma_{n/1} = 50\%$

$C = 1.85 \times 10^9\ J/m^3 \quad \delta = 0.67 \quad \rho = 7900\ kg/m^3.$

4.2. Qualitative results

Fig. 6 presents results obtained from numerical simulations. These curves enable to distinguish:

- the incubation stage, during which the material only sustains elasto-plastic deformation, without mass loss. The parameter T_i evaluated from Fig. 6a is the characteristic time of incubation stage,
- the acceleration stage, during which the mass loss begins,
- the maximum rate stage,
- followed by a deceleration phase: This is because the biggest pieces of material are removed at the beginning of the rupture process (see [41]). The same kind of curves can be found in [42].
- the terminal stage, during which the mass loss rate is constant, related to the steady-state erosion rate $\dot{E}$.

The typical curve presented in Fig. 6b enables to define the steady-state erosion rate $\dot{E}$, which is the mass loss per time unit during the terminal (or steady) period. This parameter can be useful to estimate material working life under given cavitation conditions.

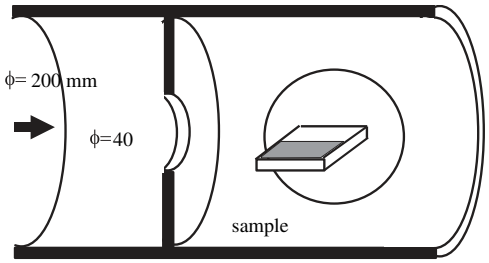

Fig. 5. Modulab test rig (Electricité de France): the diaphragm generates wake-cavitation; vapor structures are convected downstream the orifice and their collapses damage the samples [3].

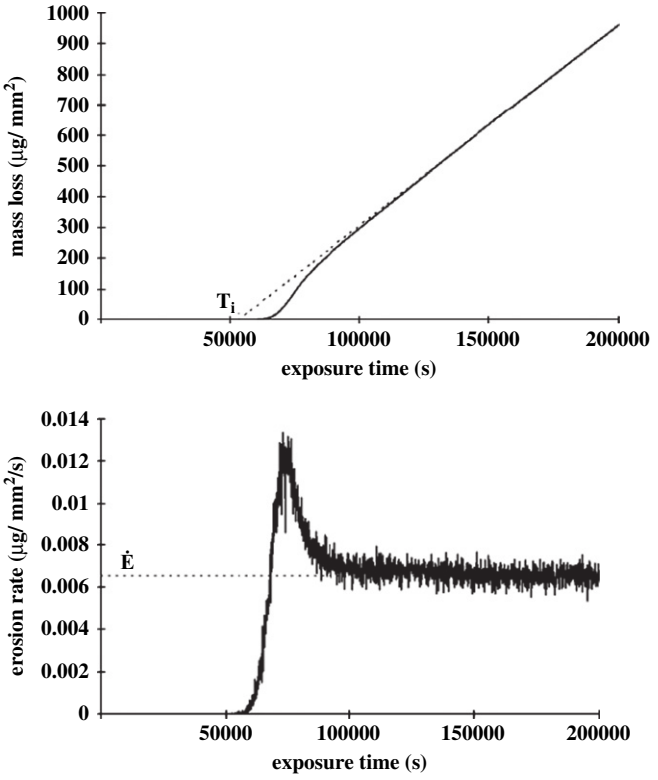

Fig. 6. (a) Mass loss (up) and (b) erosion rate (down) calculated as a function of the exposure time. Simulations are based on Al234 pitting test (Table 2). The value of the incubation time T_i is obtained from (a) as indicated in the figure. The steady-state erosion rate $\dot{E}$ is obtained from (b). The value of the volumic erosion rate V_{er} is calculated from $\dot{E} = \rho V_{er}$ (see Eq. (19)).

5. Influence of model parameters

From equations presented in Section 3 describing the applied physical model, the damage increment at a point (r,z) of the simulated material sample is given by the correlation

$$\delta D(r,z) = \left(\frac{\eta_{solid/wave}\gamma_{n/1}\beta}{C} \cdot \frac{3{,}6\{f(\lambda)\}^3 g(r)g(z)V_{pit}}{10\lambda R_{10\%}^3} \right)^{\frac{1}{\delta}} \tag{16}$$

Analyses of influence parameters have been carried out based on three parameters

$$\chi = \frac{\eta_{solid/wave}\gamma_{n/1}\beta}{C},$$

$$\lambda \text{ and } \delta. \tag{17}$$

The parameters χ and δ are related to the material properties (they are constant for a given solid material).

δ is the exponent of the fatigue energy criterion. According to results found in literature, for example in [38], δ values may vary in the range $0.6 \le \delta \le 0.7$ for metals.

χ includes material fatigue coefficient "C", hardening parameter "$\gamma_{n/1}$", and coefficients regarding the interaction between pressure wave and the solid material ($\eta_{solid/wave}$ and β). These last parameters have been introduced in Section 2 and are part of the physical scenario proposed in Fig. 1.

The parameter $\lambda = C_{liq}dt/L$ represents the dimensionless passage time of the pressure wave responsible for the material damage (see Fig. 1). At the present time, no experimental data concerning neither pressure wave passage time "dt" or the emission centre "L" are available. We consider in this study the amplitudes for "dt" and "L" given in [1].

5.1. Influence of χ

The influence of the parameter χ on the evaluation of steady-state erosion rate $\dot{E}$ and incubation period (or incubation stage) T_i has been studied using mass loss simulations based on three aluminium pitting tests results. For this study, we fixed $\lambda=12$. For a constant λ value, the spatial distribution of the damage increment is constant, but its intensity depends on χ and δ values (Eq. (16)).

According to results obtained for $\delta=0.67$ (Fig. 7) and $\delta=0.6$, the influence of χ can be expressed by the relationships

$$\dot{E} \approx \dot{E}_0 \left(\frac{\chi}{\chi_0}\right)^{\frac{1}{\delta}} \quad T_i \approx T_{i0} \left(\frac{\chi}{\chi_0}\right)^{-\frac{1}{\delta}} \tag{18}$$

These correlations allow, from given values of $\dot{E}_0$ and T_{i0} corresponding to a material characterized by (χ_0,δ), the evaluation of the magnitude order of $\dot{E}$ and T_i concerning another material characterized by (χ,δ) and exposed to the same cavitating flow.

5.2. Influence of λ

This study was carried out for fixed values $\chi=1.3$ and $\delta=0.67$. Fig. 8 points out the relevant influence of the parameter λ on results obtained. The modification of λ value leads to a variation on the damage increment intensity as well as on its spatial distribution. As a matter of fact, the maximum radius r_{max} and maximum depth z_{max} affected by plastic deformation due to pressure wave impact depend on the λ value (see Fig. 3 and Eqs. (8) and (9)).

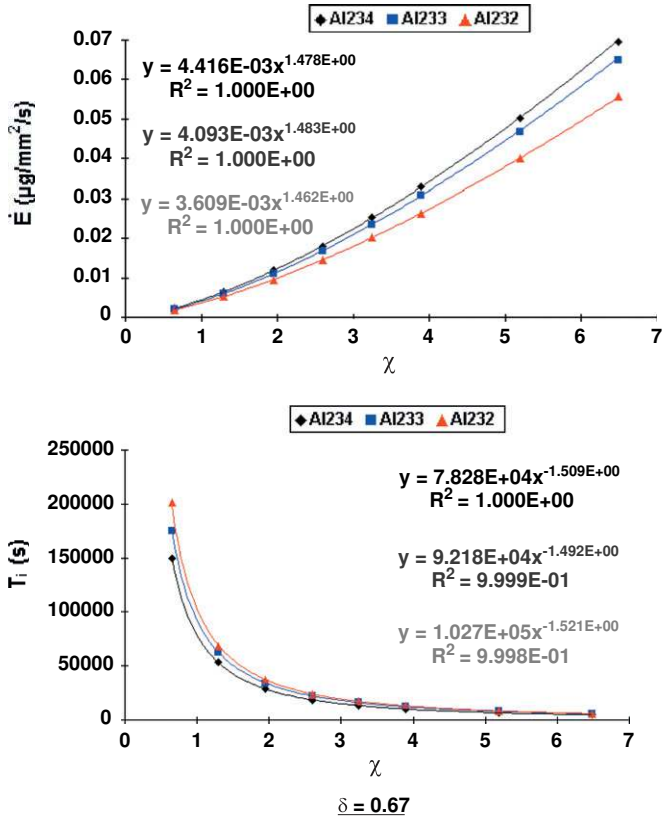

Fig. 7. Influence of parameter χ on $\dot{E}$ and on T_i. Simulations are based on pitting tests presented in Table 2. The quantitative discrepancies observed in figures are due to the influence of exposure time on pitting experimental data (see Table 2). In spite of this, we can observe a clear trend of the results for the steady-state erosion rate $\dot{E}$ and the incubation time T_i as a function of the parameter χ: $\dot{E} \approx (\chi)^{\frac{1}{\delta}}$ and $T_i \approx (\chi)^{-\frac{1}{\delta}}$.

For the moment, there is not experimental possibility to evaluate this parameter. We consider for simulations a value equal to 12. In the future, this parameter should be calibrated by comparisons between calculations and experiments.

6. Pitting rate and volumic erosion rate

With the purpose to predict, from short duration tests, the long time behavior of different materials submitted to cavitation erosion, we have analysed the relationship between pitting and erosion rates. From pitting tests obtained by EdF(R&D) in the MODULAB test rig [3], and making use of the simulation tool presented here above, calculations have been performed in order to compare pitting rate V_d and volumic erosion rate V_{er}.

The pitting rate V_d (i.e., the total volume damage per analysed surface and per exposure time), was measured by pitting tests on 316L SS, copper 99.99% and aluminium 1050A samples exposed to different cavitation conditions (Table 1). This parameter is related to incubation period of cavitation erosion phenomenon and concerns material elasto-plastic deformation.

The volumic erosion rate V_{er} is given as a function of the steady-state erosion rate $\dot{E}$ and the material specific mass by the relationship

$$V_{er} = \dot{E}/\rho \tag{19}$$

This parameter is related to terminal stage of cavitation erosion phenomenon and represents material mass loss (see Fig. 6).

Based on numerical simulations, we could evaluate V_{er} from pitting tests. Results obtained concerning the relationship between both rates are illustrated in Fig. 9. They plot the evolution of the V_{er}

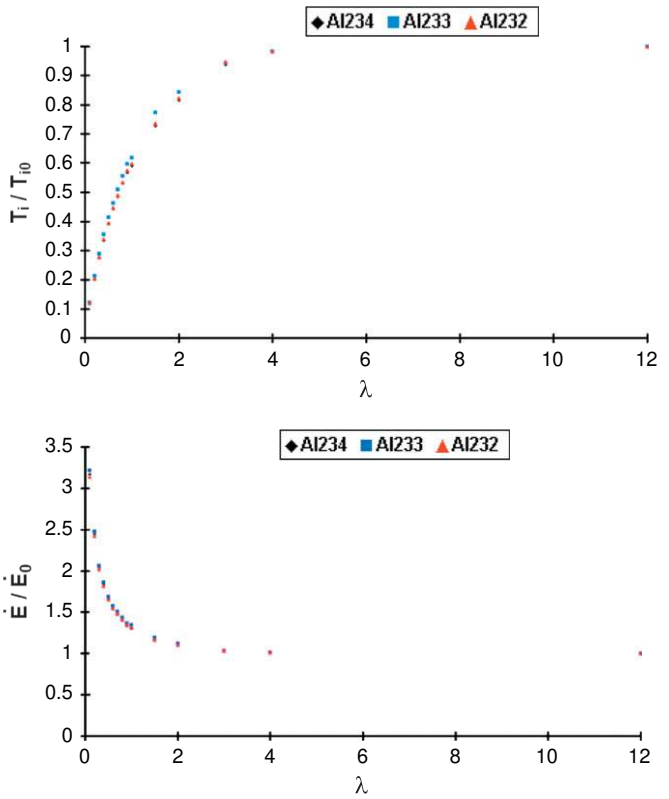

Fig. 8. Influence of the parameter λ on the evaluation of $\dot{E}$ and T_i. Values are given as a function of $\dot{E}_0$ and T_{i0} corresponding to $\lambda=12$. Simulations are based on pitting tests presented in Table 2. We can observe a clear trend of the results for the steady-state erosion rate $\dot{E}$ and the incubation time T_i as a function of the parameter λ: when $\lambda<3$, T_i increases with λ, while $\dot{E}$ decreases. The variations of erosion rate and incubation time are smaller than 5% for $\lambda>3$.

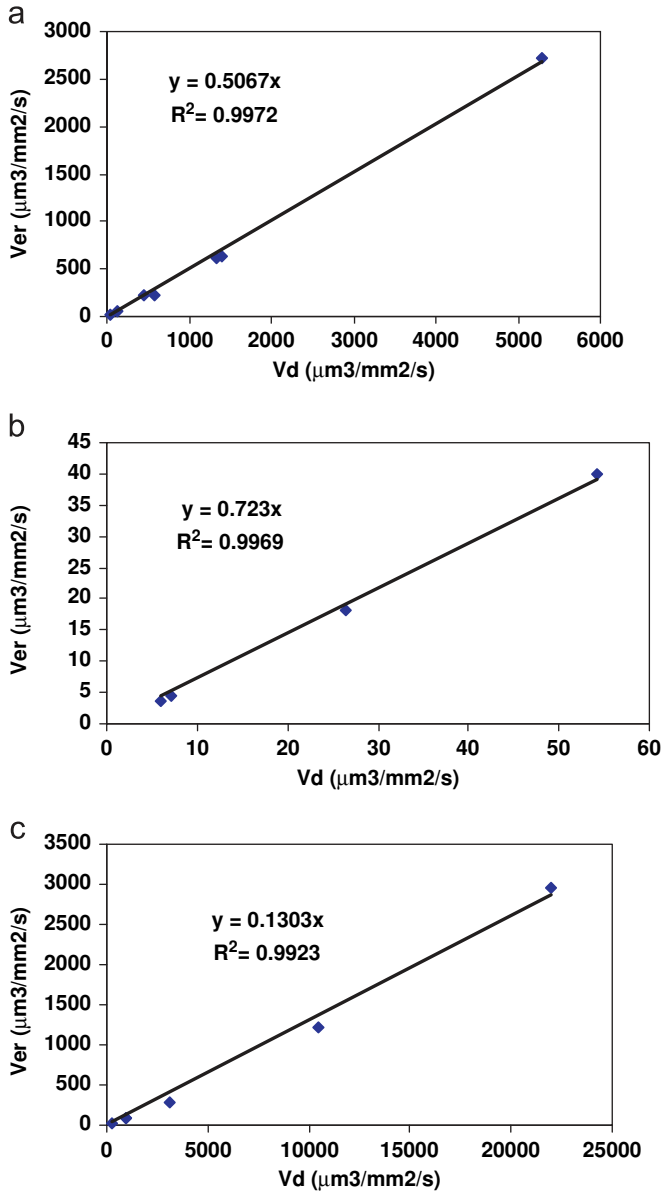

Fig. 9. Volumic erosion rate V_{er} (simulated) as a function of pitting rate V_d (measured) for samples exposed to different cavitating flows: (a) copper; (b) 316L stainless steel; (c) aluminium Pitting rates V_d are evaluated from pitting tests (Section 4.1). Experimental values of pit radius $R_{10\%}$ and volume V_{pit} are applied as input data of fatigue numerical code (Eq. (16)). The code simulates transient and steady-state stages of cavitation erosion (Fig. 6). The erosion rate V_{er} can be evaluated from this numerical result. According to the present study, the ratio V_{er}/V_d seems to be roughly constant for a given material.

$$\frac{V_{er}}{V_d}\ (\text{Copper}) \approx 0.5; \quad \frac{V_{er}}{V_d}\ (316\text{L}) \approx 0.7; \quad \frac{V_{er}}{V_d}\ (\text{alum}) \approx 0.13$$

calculated as a function of measured V_d. Calculations have been done by considering $\lambda = 12$ and material characteristics below

Copper 99.99%: $\chi = 6{,}7$; $\delta = 0.6$ and $\rho = 8100$ kg/m^3
Stainless steel 316L SS: $\chi = 6{,}5$; $\delta = 0.67$ and $\rho = 7900$ kg/m^3
Aluminium 1050A: $\chi = 2.1$; $\delta = 0.6$ and $\rho = 2700$ kg/m^3

From this study, it appears a linear dependence between V_d and V_{er} for the three materials analysed. It is worth noting that the proportionality factors depend on considered material characteristics and on accuracy of available pitting tests, mainly on evaluation of pitting rate V_d. See more details in [3]. Table 1 presents also the influence of the flow velocity on the ratio V_{er}/V_d.

Results obtained are in very good agreement with experimental works presented by [43], who observed also a constant ratio between V_d and V_{er} for high flow velocities in the case of stainless steel samples damaged in a Venturi geometry. For example, for 316L stainless steel, they found $0.2 < V_{er}/V_d < 0.25$ and for CuAl and 13/4 stainless steel: $V_{er}/V_d \approx 0.5$.

These tendencies remain to be confirmed by other coupled experimental/numerical studies.

7. Comparison between numerical predictions and experimental measurements

To validate the proposed model, we have considered experimental data corresponding to a mass loss test performed in the MODULAB test rig on aluminium samples with flow velocity equal to 38.5 m/s [44]. The incubation time was found to be in the order of 2 h, after which the steady-state mass loss rate was about 0.012 µg/mm^2/s.

The list of indentations used for the calculations was obtained on the same test rig, during pitting tests on an aluminium sample (test "al106" on Table 1–Fig. 10).

Fig. 11 present results obtained using numerical simulations. Calculations have been done by considering $\lambda = 12$, $\chi = 3.1$, $\delta = 0.6$ and $\rho = 2700$ kg/m^3. The predictions indicate an incubation period of 3 h 30 min and a steady-state mass loss rate of about 0.0125 µg/mm^2/s. These initial results are very promising and represent a first step toward validating the proposed model.

8. Conclusion

An original cavitation erosion model based on fatigue criterion has been proposed and implemented in order to predict the mass loss thanks to data provided by pitting tests.

The model considers a 2D-axisymetric approach and takes into account dynamic elasto-plastic behaviour of the material exposed

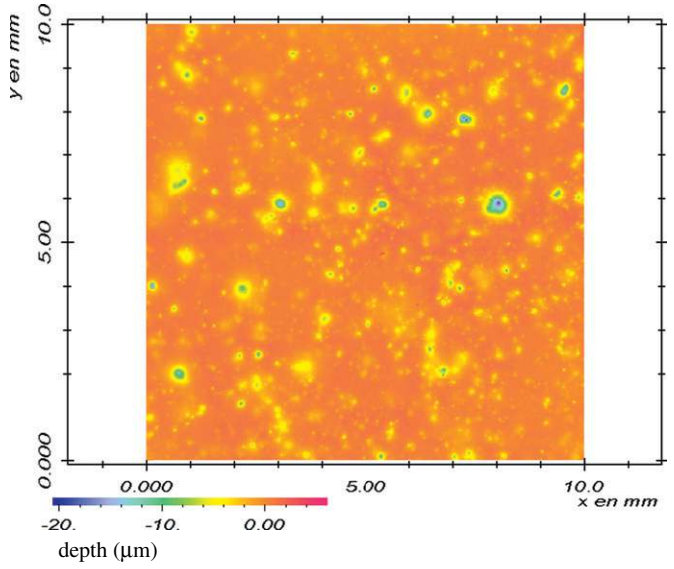

Fig. 10. Results of pitting tests obtained by 3D laser profilometry : Visualization of the surface of the aluminium sample exposed to cavitating flow during $T = 21$ s (water flow velocity = 38.5 m/s). The measurement parameters are: the analyzed area (10 mm by 10 mm); the spatial resolution (100 points/mm); and the measurement velocity (200 points/s).

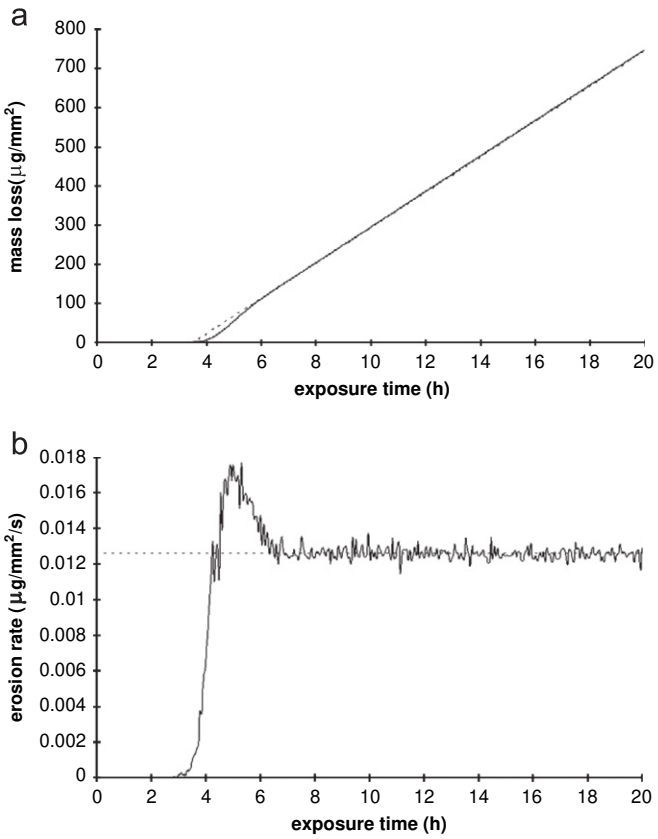

Fig. 11. (a) Mass loss (up) and (b) erosion rate (down) calculated as a function of the exposure time from "al106" pitting tests. The sample has been simulated by a $105 \times 105 \times 50$ points volume corresponding to a 10 mm^2 surface and a 368 μm depth; the step at the surface is 30 μm in both directions, and the step in depth is 7.5 μm.

to pressure wave impacts. It can be used to simulate the incubation, acceleration, maximum rate, deceleration and terminal stages of the cavitation erosion phenomenon. More particularly, steady-state erosion rate $\dot{E}$ and incubation period T_i can be evaluated from numerical simulations.

In this model, material is characterized by parameters χ and δ, related to material fatigue behaviour and to energy transfer mechanisms between material and pressure waves. The model includes the dimensionless parameter $\lambda = C_{liq} \times dt/L$ to characterize fluid medium and pressure wave emitted during bubble collapse. Experimental works allowing evaluating this characteristic parameter are not available. Moreover, another problem that we face when trying to use the proposed erosion model is the lack of material data: Energy criterion for fatigue damage is rarely used. Consequently, it is very difficult to find in literature, and specific tests should be done to get the required values.

In order to evaluate the influence of model parameters on performed simulation, many numerical tests have been carried out and could be used to estimate the results variations.

Based on numerical simulations, a complementary study has been done, which pointed out the proportionality between material damage observed during incubation period (pitting rate) and mass loss of the material exposed to cavitating flows during a long exposure time (erosion rate).

Initial results obtained by numerical calculations are promising. Qualitative results obtained for erosion rate curves are in very good agreement with experimental observations. Good quantitative results regarding incubation time and steady-state erosion rate evaluation are possible by calibrating the limited number of model parameters.

Acknowledgments

The authors wish to express their gratitude to the CETIM for supplying experimental results. This research was supported by EDF R&D and by a doctoral grant from "Ministère de l'Education Nationale", France.

References

[1] R. Fortes-Patella, J.L. Reboud, A new approach to evaluate the cavitation erosion power, Journal of Fluids Engineering—Transactions of ASME 120 (1998), June 1998.

[2] R. Fortes-Patella, J.L. Reboud, 1998, Energetical approach and impact efficiency in cavitation erosion, in: Proceedings of the Third International Symposium. on Cavitation, Grenoble.

[3] R. Fortes Patella, J.L. Reboud, A. Archer, Cavitation damage measurements by 3D laser profilometry, Wear 246 (2000) 59–67.

[4] R. Fortes Patella, G. Challier, J.L. Reboud, A. Archer, 2001, Cavitation erosion mechanism: numerical simulations of the interaction between pressure waves and solid boundaries, in: Proceedings of CAV 2001 Symposium, June 2001, Pasadena.

[5] R. Fortes Patella, G. Challier, J.L. Reboud, A. Archer, 2012, "Energy balance in cavitation erosion: from bubble collapse to indentation of material surface,-surface", J. Fluids Eng. - Trans ASMEJournal of Fluids Engineering.—Transactions of ASME, Vol. 135, 011303-1 to 11, January 2013.

[6] T. Choffat, R. Fortes-Patella, J.P. Franc, A. Archer 2003, A procedure to account for overlapping in pitting tests, in: Proceedings of CAV 2003 Symposium, November 2003, Osaka.

[7] A. Thiruvengadam, H.S. Preseir, On testing materials for cavitation damage resistance, Journal of Ship Research 1964 (8) (1964) 39.

[8] J.Z. Lichtman E.R. Weingram, 1964, The use of a rotating disk apparatus in determining cavitation erosion resistance in materials, in: J.W. Holl, G.M. Wood (Eds.), Proceedings of Symposium on Cavitation Research Facilities Technology, ASME, New York, pp. 185–196.

[9] F.J. Heymann, Toward quantitative prediction of liquid impact erosion. Characterization and determination of erosion resistance, ASTM, STP 474, American Society for Testing and Materials, Philadelphia, PA, 1970, pp. 212–248.

[10] H. Kato, A consideration on scaling laws of cavitation erosion, International Shipbuilding Progress 22 (253) (1975) 305–327.

[11] Hammitt, Cavitation erosion: the state of the art and predicting capability, Applied Mechanics Reviews 32 (1979) 6.

[12] H. Kato, 1983, Cavitation Erosion in Hydraulic Machineries, IAHR Monograph on Cavitation, September 1983, Moscow.

[13] P.V. Rao, H. Buckley, Predictive capability of long-term cavitation and liquid impingement erosion models, Wear 94 (1984) 259–274.

[14] C.J. Heathcock, et al., Cavitation erosion of stainless steels, Wear 81 (1982) 311–327.

[15] A. Ball, On the importance of work hardening in the design of wear-resistant materials, Wear 91 (1983) 201–207.

[16] S. Hattori, R. Ishikura, Q. Zhang, Construction of database on cavitation erosion and analyses of carbon steel data, Wear 257 (2004) 1022–1029.

[17] A. Karimi, W.R. Leo, Phenomenological model for cavitation erosion rate computation, Materials Science and Engineering 95 (1987) 1–14.

[18] J.P. Franc, Incubation time and cavitation erosion rate of work-hardening materials, Journal of Fluids Engineering.—Transactions of ASME 131 (2009) 021303.

[19] R.T. Knapp, Recent investigations of cavitation and cavitation damage, Transactions of ASME 77 (1955).

[20] J.P. Franc, M. Riondet, A. Karimi, G.L. Chahine, Impact load measurements in an erosive cavitating flow, Journal of Fluids Engineering—Transactions of ASME 133 (12) (2011) 121301–121308.

[21] J.P. Franc, M. Riondet, A. Karimi, G.L. Chahine, Material and velocity effects on cavitation erosion pitting, Wear 274–275 (2012) 248–259.

[22] M. Dular, B. Bachert, B. Stoffel, B. Sirok, Relationship between cavitation structures and cavitation damage, Wear 257 (2004) 1176–1184.

[23] C. Flageul, R. Fortes Patella, A. Archer, 2012, Cavitation erosion prediction by numerical simulations, in: Proceedings of 14th International Symposium on Transport Phenomena and Dynamics of Rotating Machinery, ISROMAC-14, February, Honolulu, HI, USA.

[24] R. Fortes-Patella G. Challier, J.L. Reboud, 1999, Study of pressure wave emitted during spherical bubble collapse, in: Proceedings of ASME, FEDSM99-6756, July 1999.

[25] J.L. Reboud, P. Guelin, Impact response of an elastoplastic medium, Mechanics Research Communications 4 (1988).

[26] G. Challier, 2002, Mécanismes d'interactions fluide/structure et de transfert d'énergie en érosion de cavitation, Ph.D. Thesis, INPG.

[27] S.M. Ahmed, K. Hokkirigawa, R. Oba, Fatigue failure of SUS 304 caused by vibratory cavitation erosion, Wear 177 (1994) 129–137.

[28] S.M. Ahmed, Investigation of the temperature effects on induced impact pressure and cavitation erosion, Wear 218 (1998) 119–127.

[29] T. Okada, S. Hattori, M. Shimizu, A fundamental study of cavitation erosion using a magnesium oxide single crystal (intensity and distribution of bubble collapse impact loads), Wear 186–187 (1995) 437–443.

[30] S. Hattori, E. Nakao, Cavitation erosion mechanisms and quantitative evaluation based on erosion particles, Wear 249 (2002) 839–845.
[31] A. Krella, Influence of cavitation intensity on X6CrNiTi18-10 stainless steel performance in the incubation period, Wear 258 (2005) 1723–1731.
[32] A. Krella, Cavitation degradation model of hard thin PVD coating, Advances in Materials Science 10 (3) (2010). (25), September 2010.
[33] S. Hattori, T. Hirosea, K. Sugiyamab, Prediction method for cavitation erosion based on measurement of bubble collapse impact loads, Wear 269 (2010) 507–514.
[34] W. Bedkowski, G. Gasiak, C. Lachowicz, T. Lagoda, E. Macha, Relations between cavitation erosion resistance of materials and their fatigue strength under random loading, Wear 230 (1999) 201–209.
[35] C. Bathias, J.P. Baïlon, La fatigue des matériaux et des structures, Edition Hermès, London, 1997, July 1997.
[36] C. Lemaignan, La Rupture des Matériaux, EDP Sciences, 2003 2003.
[37] F. Ellyin, K. Golos, Multiaxial fatigue damage criterion, Journal of Engineering Materials and Technology 110 (1988) 63–68.
[38] J. Lemaitre, J.L. Chaboche, Mechanics of Solid Materials, Cambridge University Press, ISBN 0521477581, 1994.
[39] M.A. Miner, Cumulative damage in fatigue, Journal of Applied Mechanics.—Transactions of ASME 12 (3) (1945) 159–164.
[40] T. Choffat, 2007, Simulation des phénomènes de marquage et de perte de masse en érosion de cavitation, Ph.D. Thesis, INPG, May 2007.
[41] E.C. Fitch, Cavitation wear in hydraulic systems, Practicing Oil Analysis Magazine, Tribolics Inc., 2002.
[42] J. Steller, A. Krella, J. Koronowicz, W. Janicki, Towards quantitative assessment of material resistance to cavitation erosion, Wear 258 (2005) (2004) 604–613.
[43] B. Le Fur, J.F. David, 1998, Comparison between pitting rate and erosion rate for 3 materials, in: Third International Symposium on Cavitation, Grenoble, April 1998.
[44] R. Simoneau, A. Archer, 1997, Transposition of cavitation marks on different hardness metals, in: ASME Fluids Engineering Division Summer Meeting, June 1997.